How to Cite: Anwar, B., Febriani, L.I., Dara, F., & Yuliani, G. (2026). Biopolymer-Based Pectin/PVP/CNC Nanocomposites as Sustainable Matrices for Solid Polymer Electrolyte Systems. *Eurasian Journal of Chemistry, 31, 2(122), 4–15.* https://doi.org/10.31489/2959-0663/2-26-4

ORGANIC CHEMISTRY

Article

Received: 9 January 2026 | Revised: 27 April 2026 |
Accepted: 12 May 2026 | Published online: 19 May 2026

UDC 544.42+519.242.7

https://doi.org/10.31489/2959-0663/2-26-4

Budiman Anwar[1, 2*], Lidya I. Febriani[1], Fitri Dara[3], Galuh Yuliani[1, 2]

[1]*Chemistry Programs, Universitas Pendidikan Indonesia, Bandung, Indonesia;*
[2]*ChemTransform for Sustainability Research Group, Universitas Pendidikan Indonesia, Bandung, Indonesia;*
[3]*National Research and Innovation Agency (BRIN), Bandung, Indonesia*
*(*Corresponding author's e-mail: budimananwar@upi.edu)*

Biopolymer-Based Pectin/PVP/CNC Nanocomposites as Sustainable Matrices for Solid Polymer Electrolyte Systems

Biopolymer-based solid polymer electrolytes (SPEs) are attractive as sustainable alternatives to petroleum-derived systems; however, balancing mechanical integrity and chain mobility remains challenging. In this study, cellulose nanocrystals (CNCs) were incorporated into an optimized pectin/poly(vinyl pyrrolidone) (PVP) polyblend to elucidate their role as functional nanofillers in biopolymer-based SPE matrix design. CNCs were introduced into the pectin/PVP (7:1, w/w) matrix at loadings of 2, 4, and 6 wt% via solution casting. FTIR and SEM analyses suggest good compatibility and homogeneous dispersion of CNCs through hydrogen-bond-mediated interactions. Mechanical testing shows that CNC incorporation does not function as conventional reinforcement; instead, low to intermediate CNC contents reduce stiffness and strength while enhancing ductility, indicating increased segmental mobility. DSC analysis reveals CNC-induced modulation of Tg-related enthalpy relaxation without inducing crystallinity. SEM observations further confirm a continuous polymer matrix with CNC-induced interfacial heterogeneity and no macroscopic phase separation. These findings demonstrate that CNCs function as mobility-regulating nanofillers, enabling controlled tuning of thermal–mechanical behavior, and highlight pectin/PVP/CNC nanocomposites as promising sustainable matrices for future solid polymer electrolyte systems.

Keywords: biopolymers, nanocomposite, pectin, poly(vinyl pyrrolidone), cellulose nanocrystals, solid polymer electrolyte, polyblend, sustainable polymer matrices

Introduction

The rapid growth of electrochemical energy storage technologies has intensified the demand for safe, flexible, and sustainable electrolyte materials. Among various candidates, solid polymer electrolytes (SPEs) have attracted considerable attention owing to their improved safety, mechanical integrity, and processability compared to liquid electrolytes [1]. Conventional SPE matrices are predominantly based on petroleum-derived polymers such as poly(ethylene oxide) (PEO) [2], poly(vinylidene fluoride) (PVDF) and its copolymers [3], poly(methyl methacrylate) (PMMA) [4], and poly(vinyl alcohol) (PVA) [5], which have demonstrated promising ion-transport capabilities when combined with lithium salts and suitable plasticizers. However, concerns regarding environmental sustainability, resource depletion, and end-of-life disposal have motivated the exploration of biopolymer-based alternatives.

Biopolymers derived from renewable resources, including polysaccharides and their derivatives, offer inherent advantages such as biodegradability, low toxicity, and abundant functional groups capable of coordinating ionic species [6–8]. Among these materials, pectin, a naturally occurring anionic polysaccharide, has emerged as a promising host polymer due to its film-forming ability, hydrophilicity, and rich hydroxyl and carboxyl functionalities. Nevertheless, pristine pectin films often suffer from limited mechanical strength and thermal stability, restricting their direct application as SPE matrices. To overcome these limitations, polymer blending, particularly with poly(vinyl pyrrolidone) (PVP), has been demonstrated as an effective strategy to enhance mechanical performance and compatibility through hydrogen bonding interactions [9].

Beyond polymer blending, the incorporation of nanoscale fillers has proven to be a powerful approach for tailoring the structure–property relationships of SPE matrices. In particular, cellulose nanocrystals (CNCs) have attracted increasing interest as sustainable nanofillers due to their high aspect ratio, superior mechanical stiffness, large specific surface area, and abundance of surface hydroxyl groups. Previous studies have shown that CNCs can enhance mechanical integrity, modify polymer chain mobility, and influence dielectric properties, all of which are critical parameters governing ion transport in polymer electrolytes. In addition, CNCs may act as physical crosslinking points and facilitate the formation of continuous ion-conduction pathways through polymer–filler interactions [10, 11].

Despite growing interest in CNC-containing SPE systems, most reported studies focus on synthetic polymer matrices, while biopolymer-based CNC-reinforced matrices remain relatively underexplored. In particular, systematic investigations addressing how CNC incorporation influences the mechanical, thermal, and physicochemical properties of pectin/PVP matrices—as prerequisites for SPE applications—are still scarce. Understanding these effects is essential for establishing design principles for sustainable SPE platforms that balance mechanical robustness, thermal stability, and ion-hosting capability.

Therefore, in this work, CNCs were incorporated into an optimized pectin/PVP polyblend to elucidate their role as functional nanofillers in biopolymer-based SPE matrices. Rather than focusing on ionic conductivity at this stage, this study emphasizes the structure–property relationships induced by CNC incorporation, including mechanical behavior, thermal transitions, hydrophilicity, and microstructural homogeneity, which collectively determine the suitability of the material as a solid polymer electrolyte matrix.

Experimental

Materials. Pectin extracted from citrus peel, poly(vinyl pyrrolidone) (PVP, average molecular weight 40 kDa), and glycerol were purchased from Sigma-Aldrich (Merck, Germany) and used as received. Bacterial cellulose (BC), in the form of *nata de coco* sheets, was obtained from a local commercial source and used as the precursor for cellulose nanocrystal (CNC) isolation.

Isolation of CNC. BC pellicles were dried at 70 °C for 7 h, ground into powder, and sieved to obtain a homogeneous particle size distribution. CNCs were isolated from BC via sulfuric acid hydrolysis under optimized conditions reported previously [12, 13]. Briefly, BC powder was hydrolyzed using 50 wt% sulfuric acid at a solid-to-liquid ratio of 1:50 (m/v) at 45 °C for 45 min under continuous stirring. The reaction was quenched by dilution with cold distilled water (1:10, v/v), followed by centrifugation at 4000 rpm for 10 min. The collected suspension was dialyzed against distilled water until pH ≈ 6, sonicated for 20 min at 75 % amplitude, and freeze-dried to obtain CNC powder.

Preparation of Pectin/PVP Polyblend Films. Pectin/PVP polyblend films were prepared by the solution casting method with minor modifications from reported procedures [9]. PVP and pectin were dissolved separately in distilled water, combined under stirring, and plasticized with glycerol (0.5 mL). The total polymer concentration was kept constant, while pectin/PVP weight ratios were varied at 8:0, 7:1, 6:2, and 5:3 (w/w). The resulting solutions were degassed, cast onto plastic Petri dishes, and dried at ambient conditions to obtain free-standing films.

Preparation of Pectin/PVP/CNC Nanocomposite Films. Pectin/PVP/CNC nanocomposite films were prepared by incorporating CNCs (2, 4, and 6 wt% relative to total polymer weight) into the optimized pectin/PVP matrix using solution casting. CNCs were dispersed in distilled water, stirred overnight, and ultrasonicated prior to addition into the polymer blend. The resulting ternary mixtures were homogenized, degassed, cast, and dried under ambient conditions to obtain free-standing nanocomposite films for characterization.

Fourier Transform Infrared (FTIR) Spectroscopy. FTIR spectroscopy was employed to investigate the chemical structure, intermolecular interactions, and crystallinity of BC, CNC, and polymer films. FTIR spectra of BC and CNC powders were recorded using a Bruker Alpha II FTIR spectrometer. The samples were prepared in the form of KBr pellets and analyzed over the wavenumber range of 4000–500 cm^{-1} to evaluate changes in chemical composition induced by the acid hydrolysis process.

FTIR spectra of pectin, PVP, pectin/PVP polyblend films, and pectin/PVP/CNC nanocomposite films at the optimum composition were recorded using a Shimadzu 8400 FTIR spectrometer in the frequency range of 4000–400 cm^{-1}. FTIR analysis of the film samples was performed to identify functional groups, assess changes in chemical composition, and elucidate intermolecular interactions through hydrogen bonding within the polymer matrix.

X-ray Diffraction (XRD). XRD measurements of BC and CNC powders were carried out using a diffractometer equipped with Cu Kα radiation ($\lambda = 0.154$ nm). Diffraction patterns were recorded over a 2θ range of 2–90° with a step size of 0.02°, operating at a generator voltage of 45 kV and a tube current of 40 mA. XRD analysis was employed to determine the crystallinity index (CI) and crystallite size (L) of the samples. The CI was calculated using the Segal method [14] according to Eq. (1):

$$\mathrm{CI}(\%) = \frac{I_{200} - I_{am}}{I_{200}} \times 100\,, \tag{1}$$

where I_{200} is the maximum intensity of the crystalline peak at $2\theta \approx 22.5°$, and I_{am} is the intensity of the amorphous region at $2\theta \approx 18°$. The crystallite size was estimated using the Scherrer equation (Eq. (2)) [13]:

$$\mathrm{D} = \frac{K\lambda}{\beta \cos\theta}\,, \tag{2}$$

where K is the Scherrer constant (0.94), λ is the X-ray wavelength, β is the full width at half maximum (FWHM) of the diffraction peak in radians, and θ is the Bragg angle.

Transmission Electron Microscopy (TEM). Transmission electron microscopy (TEM) was used to examine the morphology and particle size of the isolated CNCs. A drop of CNC aqueous suspension was deposited onto a carbon-coated copper grid and allowed to dry at ambient conditions prior to observation using a Hitachi HT7700 TEM. Particle dimensions were statistically determined by measuring approximately 200 individual CNC particles using the ImageJ software.

Particle Size Analysis (PSA). The particle size distribution of CNCs dispersed in distilled water was determined using a particle size analyser based on dynamic light scattering (DLS). Prior to measurement, the CNC suspension was ultrasonicated for 5 min to ensure uniform dispersion. Measurements were conducted at 25.1 °C using a refractive index of 1.30.

Scanning Electron Microscopy (SEM). The surface morphology of pectin, pectin/PVP polyblend, and pectin/PVP/CNC nanocomposite films were examined using an EVO MA 10 scanning electron microscope. Film samples were cut into specimens with dimensions of 2×2 cm^2 and observed at an accelerating voltage of 15 kV with magnifications of up to ×2000.

Tensile Test. The mechanical properties of the films, including tensile strength, elongation at break, and Young's modulus, were evaluated using a Textechno Favigraph I-PI-067 tensile testing instrument. Tensile tests were performed at a crosshead speed of 6.0 mm min^{-1} under dry conditions at room temperature. Prior to testing, all films were cut into rectangular specimens with a width of 3 mm and a gauge length of 50 mm.

Differential scanning calorimetry (DSC). The glass transition temperature (T_g) and enthalpy relaxation change (ΔH_{relax}) of the films were investigated by DSC using a NETZSCH DSC 214 Polyma instrument under a nitrogen atmosphere. Film specimens were hermetically sealed in aluminum DSC pans and heated from 25 to 250 °C at a heating rate of 10 °C min^{-1}.

Results and Discussion

The successful formation of cellulose nanocrystals (CNCs) from bacterial cellulose (BC) was confirmed through a combination of FTIR, XRD, TEM, and particle size analysis (PSA). These complementary techniques collectively verify that the acid hydrolysis process effectively transformed bulk cellulose into nanoscale crystalline domains.

FTIR spectra of bacterial cellulose (BC) and cellulose nanocrystals (CNC) exhibit the characteristic absorption bands of cellulose, including the broad O–H stretching vibration in the range of 3300–3400 cm^{-1}, C–H stretching near 2900 cm^{-1}, and C–O–C stretching vibrations between 1000 and 1150 cm^{-1} (Fig. 1). The preservation of these characteristic bands after sulfuric acid hydrolysis indicates that the fundamental chemical structure of cellulose remains intact and that no significant chemical modification of the cellulose backbone occurs during CNC isolation [13].

Compared to BC, CNC shows a noticeable reduction in the intensity and breadth of the O–H stretching band, which can be attributed to the preferential removal of disordered cellulose domains containing loosely hydrogen-bonded hydroxyl groups. A decrease in the intensity of the CH_2 bending vibration at approximately 1430 cm^{-1} is also observed for CNC. Rather than being interpreted as a direct indicator of crystallinity, this change reflects a reduction in flexible and amorphous chain segments resulting from the selective dissolution of amorphous regions during acid hydrolysis [15].

No new absorption bands appear in the CNC spectrum, confirming that sulfuric acid hydrolysis selectively removes amorphous cellulose without altering the intrinsic cellulose framework. FTIR analysis provides qualitative evidence for the elimination of disordered domains while preserving the cellulose backbone, thereby supporting the successful formation of cellulose nanocrystals. Quantitative assessment of crystallinity is therefore more appropriately derived from X-ray diffraction analysis, as discussed in the subsequent paragraphs.

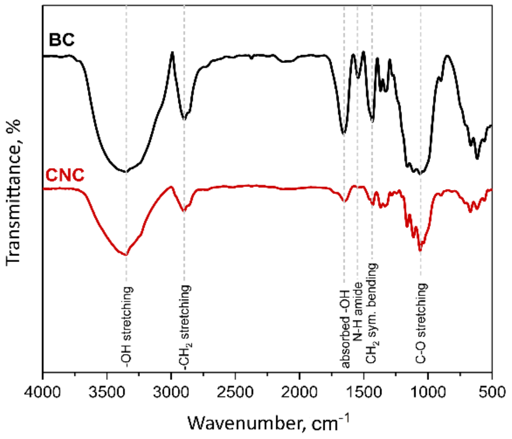

Figure 1. FTIR Spectra of BC and CNC

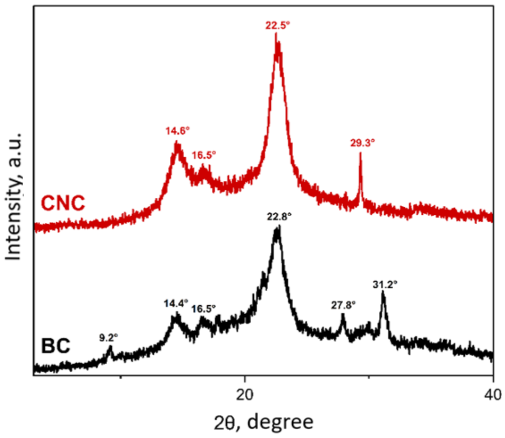

Figure 2. X-ray diffractogram of BC and CNC

XRD patterns of BC and CNC exhibit characteristic reflections of cellulose I, with diffraction peaks appearing at 2θ ≈ 14–17° and a dominant peak at 2θ ≈ 22–23°, corresponding to the $(\bar{1}10)$, (110), and (200) crystallographic planes (Fig. 2). The preservation of these diffraction features after sulfuric acid hydrolysis confirms that the native cellulose I crystalline structure remains unchanged during CNC isolation. Compared to BC, the diffraction pattern of CNC displays sharper and more intense crystalline reflections, particularly for the (200) plane, indicating a higher degree of structural ordering. This observation is consistent with the preferential removal of amorphous cellulose domains during acid hydrolysis, resulting in the enrichment of crystalline regions within the CNC structure [13, 16].

In addition to changes in crystallinity, the crystallite size, estimated using the Scherrer equation, shows an apparent increase after hydrolysis. The increase in crystallite size suggests that acid hydrolysis effectively removes disordered regions surrounding the crystalline domains, leading to more well-defined and coherent crystalline segments [17, 18]. The calculated values of crystallinity index (Eq. 1) and crystallite size (Eq. 2) for both BC and CNC are summarized in Table 1.

Importantly, no additional diffraction peaks or phase transformations were observed after hydrolysis, confirming that the acid treatment selectively removes disordered regions without altering the intrinsic crystalline form of cellulose. These XRD results provide quantitative evidence supporting the FTIR findings, demonstrating that sulfuric acid hydrolysis effectively converts bacterial cellulose into cellulose nanocrystals with higher crystallinity while maintaining the cellulose I crystal structure.

Table 1

Crystallinity index (CI) and crystallite size (*L*) of BC and CNC

Sample	CI, %	L_{200}, nm
BC	62	4.93
CNC	80	5.48

The morphology and size characteristics of the isolated CNCs were analyzed using TEM and PSA to provide complementary information on their physical dimensions. TEM images (Fig. 3*a*) show that the CNCs exhibit a rod-like (needle-shaped) morphology, which is typical for nanocrystalline cellulose obtained via sulfuric acid hydrolysis. The nanocrystals appear well separated, indicating effective removal of the amorphous regions of bacterial cellulose and the release of individual crystalline domains.

Quantitative analysis based on TEM images (Figs. 3*b* and 3*c*) reveals that the CNCs possess an average length of 714 ± 12 nm and an average diameter of 31 ± 0.2 nm, resulting in a high aspect ratio (L/D) of ~ 23. Such a high aspect ratio is a defining characteristic of cellulose nanocrystals and is indicative of their rigid, anisotropic nature. These dimensions confirm that the hydrolysis process successfully produced nanocrystals rather than nanofibrillated or microcrystalline cellulose.

The particle size distribution obtained from PSA measurements (Fig. 3*d*) shows an average particle diameter of 80 ± 22 nm, which is larger than the diameter determined by TEM. This difference is expected, as PSA based on dynamic light scattering measures the hydrodynamic diameter of particles in suspension, which is influenced by solvation layers, particle orientation, and possible interparticle interactions. In contrast, TEM provides direct measurements of the physical dimensions of individual nanocrystals in the dry state.

While TEM analysis shows a Gaussian distribution (Fig. 3*c*) corresponding to the actual geometric dimensions of CNCs, the DLS-derived number distribution exhibits a positively skewed profile (Fig. 3*d*). This difference arises from the hydrodynamic nature of DLS measurements and the anisotropic morphology of CNCs, and therefore a Gaussian distribution is not necessarily expected for DLS data.

The combined TEM and PSA results consistently confirm the formation of well-defined cellulose nanocrystals with nanoscale dimensions and high aspect ratio, validating the effectiveness of sulfuric acid hydrolysis in converting bacterial cellulose into CNCs.

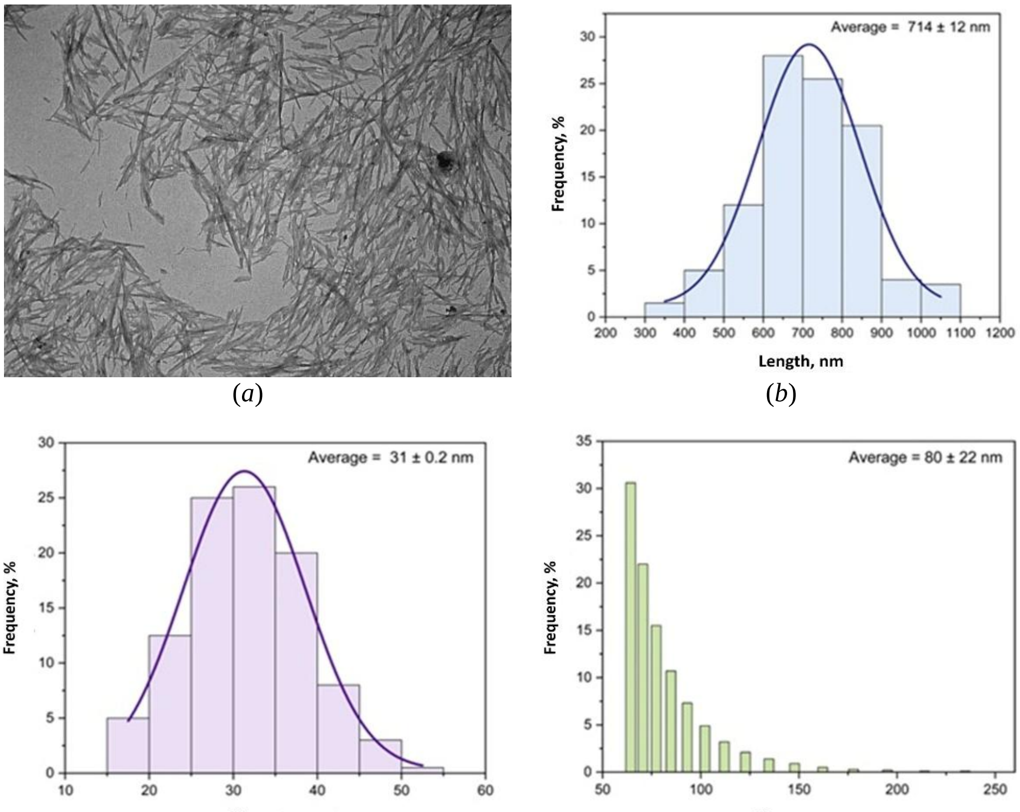

(*a*) (*b*)

(*c*) (*d*)

Figure 3. (*a*) TEM image of CNCs, (*b*) length and (*c*) diameter distribution of CNCs based on TEM, (*d*) diameter distribution of CNCs obtained from PSA

The mechanical properties of pectin/PVP polyblend films with different compositions were systematically evaluated to identify an optimal matrix for subsequent CNC incorporation. As summarized in Table 2, the mechanical response of the films shows a noticeable dependence on the PVP content, reflecting the balance between intermolecular interactions and plasticization effects. Neat pectin films (8:0) exhibit moderate tensile strength but limited flexibility, indicative of a relatively stiff and brittle polysaccharide network.

The incorporation of a small amount of PVP (7:1, w/w) leads to an observable improvement in overall mechanical performance, characterized by simultaneous enhancement of tensile strength and elongation at break. This synergistic behavior can be attributed to strong intermolecular hydrogen bonding between the hydroxyl groups of pectin and the carbonyl groups of PVP, which promotes good miscibility and efficient stress transfer while preserving sufficient chain mobility. Similar structure–property relationships have been reported for polysaccharide/PVP blends, where optimal PVP content maximizes mechanical performance through hydrogen-bond-driven miscibility without excessive plasticization [19].

Table 2

Mechanical properties of pectin and pectin/PVP blend films

Pektin/PVP composition, w/w	Film thickness, μm	Tensile strength, Mpa	Elongation at break, %	Young's modulus, MPa
8:0	101 ± 4	27.9 ± 4.3	13.4 ± 2.3	222.4 ± 96.0
7:1	93 ± 4	30.5 ± 5.7	17.5 ± 2.8	1702.4 ± 93.1
6:2	106 ± 6	27.1 ± 6.4	15.2 ± 1.6	194.4 ± 67.4
5:3	100 ± 2	28.6 ± 5.7	12.9 ± 2.7	112.1 ± 45.8

At higher PVP contents (6:2 and 5:3), the mechanical properties deteriorate, as evidenced by reduced tensile strength, elongation at break, and modulus. In this system, the plasticization effect is primarily attributed to PVP (40 kDa), which enhances chain mobility by disrupting pectin–pectin interactions. However, at higher PVP contents, excessive incorporation leads to over-plasticization, where the disruption of cohesive pectin–pectin interactions becomes dominant [20, 21]. This results in reduced intermolecular cohesion and weakened mechanical integrity, indicating a balance between plasticization and structural weakening of the polymer network [22]. Consequently, the pectin/PVP composition of 7:1 (w/w) provides the most balanced combination of strength and flexibility and was therefore selected as the optimum matrix for CNC incorporation. Figure 4 displays a photograph of pectin, pectin/PVP, and pectin/PVP/CNC films.


(*a*) (*b*) (*c*)

Figure 4. Photograph of (*a*) pectin, (*b*) pectin/PVP (7:1), and (*c*) pectin/PVP/CNC 6 % films

The effect of CNC incorporation on the mechanical properties of the optimized pectin/PVP (7:1, w/w) matrix was evaluated at CNC loadings of 2, 4, and 6 wt% (Tab. 3). The neat pectin/PVP film (0 % CNC) exhibits a relatively high tensile strength and Young's modulus with moderate elongation at break, indicating a mechanically robust polyblend network.

Table 3

Mechanical properties of pectin/PVP/CNC films

CNC composition, %	Film thickness, μm	Tensile strength, Mpa	Elongation at break, %	Young's modulus, MPa
0	93 ± 4	30.5 ± 5.7	17.5 ± 2.8	1702.4 ± 93.1
2	105 ± 14	10.2 ± 0.3	17.7 ± 5.9	117.6 ± 61.8
4	117 ± 2	9.2 ± 1.8	24.5 ± 6.2	59.4 ± 15.4
6	108 ± 4	13.8 ± 2.5	15.0 ± 3.4	123.0 ± 51.0

Upon CNC addition, a pronounced reduction in tensile strength and modulus is observed, particularly at 2–4 wt% CNC. At 2 wt% CNC, tensile strength decreases to 10.2 ± 0.3 MPa and modulus to 117.6 ± 61.8 MPa, while elongation remains comparable to the CNC-free film. At 4 wt% CNC, the film shows the highest ductility with elongation increasing to 24.5 ± 6.2 %, accompanied by the lowest modulus (59.4 ± 15.4 MPa) and reduced tensile strength (9.2 ± 1.8 MPa). This trend suggests that, within this loading range, CNC incorporation does not act as a conventional reinforcing filler; instead, it likely disrupts the cohesive pectin–PVP network and introduces interfacial regions that facilitate chain mobility, resulting in a more compliant and extensible film [23].

Interestingly, at 6 wt% CNC, the tensile strength partially recovers to 13.8 ± 2.5 MPa and the modulus increases to 123.0 ± 51.0 MPa, while elongation decreases to 15.0 ± 3.4 %. The partial recovery at higher CNC loading may indicate the onset of a more effective filler contribution, potentially due to increased filler–matrix contacts and the formation of a percolated rigid phase that restricts deformation. Nevertheless, the overall decrease in strength and stiffness compared to the neat polyblend implies that CNC dispersion state and interfacial compatibility dominate the mechanical response of the nanocomposites.

FTIR spectroscopy was employed to elucidate the intermolecular interactions within the pectin/PVP matrix and to examine the effect of CNC incorporation on the chemical environment of the polymer films (Fig. 4). The spectrum of neat pectin (Fig. 5*a*) exhibits a broad O–H stretching band centered at ~3406 cm^{-1}, characteristic of extensive hydrogen bonding in polysaccharide networks. The absorption near 2924 cm^{-1} corresponds to C–H stretching, while the band at ~1626 cm^{-1} is associated with asymmetric stretching of carboxylate groups. The strong absorption in the range of 1000–1150 cm^{-1} originates from C–O–C and C–O stretching vibrations of the polysaccharide backbone [24].

Pure PVP (Fig. 5*b*) shows a distinct absorption band at ~1659 cm^{-1}, attributed to the C=O stretching of the pyrrolidone ring (amide I), along with C–H stretching around 2955 cm^{-1} and characteristic bands in the 1280–1300 cm^{-1} region corresponding to C–N stretching. These features confirm the presence of carbonyl groups capable of acting as strong hydrogen-bond acceptors [25].

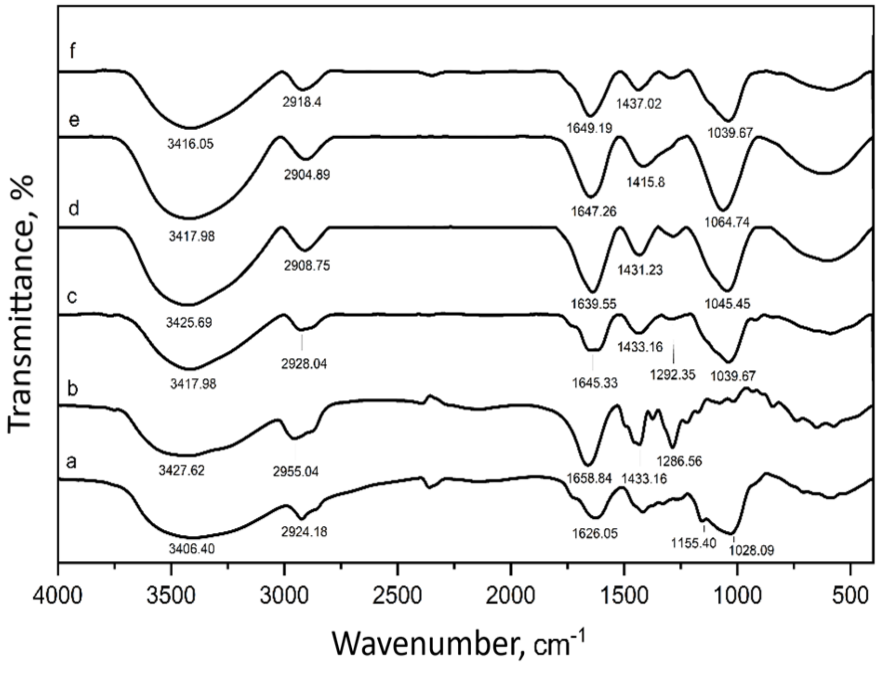

Figure 5. FTIR spectra of (*a*) pectin, (*b*) PVP, (*c*) pectin/PVP, (*d*) pectin/PVP/CNC 2 %, (*e*) pectin/PVP/CNC 4 %, and (*f*) pectin/PVP/CNC 6 %

Upon blending pectin with PVP (Fig. 5*c*), noticeable spectral changes are observed in the O–H stretching region. The broad O–H band of neat pectin centered at ~3406 cm^{-1} (Fig. 4*a*) shifts to a higher wavenumber (~3418 cm^{-1}) in the pectin/PVP film and becomes narrower and sharper. This blue shift and band narrowing suggest a more uniform hydrogen-bonding environment and a redistribution of hydroxyl interactions, consistent with reduced heterogeneity of the polysaccharide hydrogen-bond network upon PVP incorporation [26]. In parallel, the carbonyl stretching band of PVP around ~1659 cm^{-1} (Fig. 4*b*) shifts to ~1645 cm^{-1} in the polyblend (Fig. 4*c*), indicating specific interactions between the PVP carbonyl groups and pectin hydroxyl/carboxyl functionalities. Together, these spectral changes support good polymer–polymer compatibility mediated by hydrogen bonding, which is consistent with the improved mechanical balance observed for the pectin/PVP (7:1) matrix.

Following CNC incorporation into the pectin/PVP matrix (Fig. 5*d-f*), further systematic changes are observed in the O–H stretching region. Compared to the pectin/PVP film, the O–H band remains centered in the range of ~3416–3418 cm^{-1} but becomes slightly broader with increasing CNC content, reflecting the introduction of additional hydroxyl groups from the CNC surface into the hydrogen-bonding network. Unlike the pectin/PVP blend, where the O–H band is relatively narrow and sharp, the presence of CNC reintroduces a degree of heterogeneity in hydrogen bonding due to polymer–CNC and CNC–CNC interactions [26].

In addition, subtle variations are detected in the CH_2 bending region (~1430–1440 cm^{-1}) and the C–O stretching bands around 1039–1065 cm^{-1} upon CNC addition. These changes indicate physical interactions between CNC and the polymer matrix rather than the formation of new covalent bonds. The absence of new absorption bands across all CNC loadings confirms that CNC functions as a physically interacting nanofiller, primarily through hydrogen bonding.

The evolution of the hydrogen-bond-related bands provides a molecular-level explanation for the mechanical behavior of the nanocomposite films. At low to intermediate CNC loadings, the redistribution and partial heterogenization of hydrogen bonds weaken the original pectin–PVP cohesive network, resulting in reduced tensile strength and modulus but enhanced ductility. At higher CNC content, the increased density of polymer–CNC interactions contributes to partial restriction of chain mobility, which is consistent with the observed recovery in mechanical stiffness. The FTIR results corroborate that hydrogen-bond-mediated interactions govern the balance between mechanical compliance and rigidity in the pectin/PVP/CNC nanocomposites.

The DSC thermograms of pectin, pectin/PVP, and pectin/PVP/CNC films (Fig. 6) exhibit two distinct thermal events. The dominant thermal transition is a broad endothermic peak observed in the range of ~70–100 °C, which is assigned to enthalpy relaxation (ΔH_{relax}) related to the glass transition region, strongly influenced by the release of bound water and the rearrangement of hydrogen-bonded polymer chains. A secondary endothermic event observed at higher temperatures (~210–240 °C) is associated with further molecular relaxation or the onset of structural rearrangement prior to thermal degradation, rather than crystalline melting.

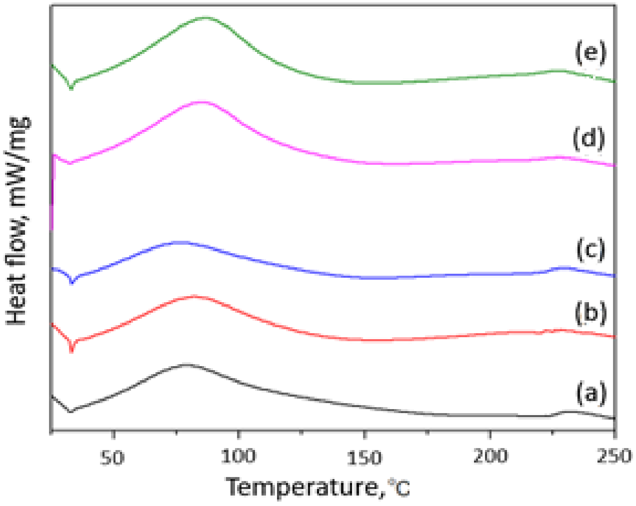

Figure 6. Thermogram DSC of (*a*) pectin, (*b*) pectin/PVP, (*c*) pectin/PVP/CNC 2 %,
(*d*) pectin/PVP/CNC 4 %, and (*e*) pectin/PVP/CNC 6 % films

Quantitative DSC parameters derived from the thermograms (Fig. 6) are summarized in Table 4, including the apparent glass transition temperature (T_g) and ΔH_{relax}. It should be noted that, in hydrophilic biopolymer systems, the reported T_g values correspond to the temperature region of enthalpy relaxation rather than a classical baseline step change, due to the strong influence of bound water and hydrogen-bond rearrangement [27, 28].

Neat pectin exhibits a T_g-related relaxation at 78.9 °C with a relatively high ΔH_{relax} of 308.3 J g^{-1}, indicating a rigid polysaccharide network with limited segmental mobility and a high degree of internal stress stored during film formation. Upon blending with PVP, the T_g shifts to a higher temperature (82.5 °C), while ΔH_{relax} decreases substantially to 225.5 J g^{-1}. This reduction in relaxation enthalpy suggests a more homogeneous and dynamically equilibrated polymer network, consistent with hydrogen-bond-driven miscibility between pectin and PVP and the improved mechanical balance observed for the polyblend.

Table 4

Thermal properties of pectin, pectin/PVP, and pectin/PVP/CNC

Data	Pectin	Pectin/PVP	Pectin/PVP/CNC 2 %	Pectin/PVP/CNC 4 %	Pectin/PVP/CNC 6 %
T_g, °C	78.9	82.5	76.3	84.4	86.5
ΔH_{relax}, J/g	308.3	225.5	188.4	324.9	318.8

The incorporation of CNC further modulates the thermal relaxation behavior. At 2 wt% CNC, the T_g decreases to 76.3 °C, accompanied by a pronounced reduction in ΔH_{relax} (188.4 J g^{-1}). This combination indicates enhanced chain mobility and reduced structural constraints, which can be attributed to the disruption of the pectin/PVP hydrogen-bond network by polymer–CNC interfacial interactions. Such behavior is consistent with the increased ductility observed in mechanical testing at low CNC loading.

At higher CNC contents (4 and 6 wt%), T_g shifts progressively to higher temperatures (84.4 and 86.5 °C, respectively), while ΔH_{relax} increases to 324.9 and 318.8 J g^{-1}. The increase in T_g reflects partial restriction of polymer chain motion due to the higher density of polymer–CNC interactions, whereas the elevated ΔH_{relax} indicates the development of a more heterogeneous hydrogen-bonding network with increased stored relaxation energy. This trend correlates with the partial recovery of mechanical stiffness at higher CNC loading [29].

Scanning electron microscopy was employed to examine the surface morphology of neat pectin, pectin/PVP polyblend, and pectin/PVP/CNC nanocomposite films (Fig. 7). The SEM micrograph of neat pectin shows a relatively rough and heterogeneous surface, characterized by irregular features and micro-scale undulations. This morphology reflects the rigid and highly hydrogen-bonded polysaccharide network of pectin, which is consistent with its limited ductility and higher brittleness observed in mechanical testing.

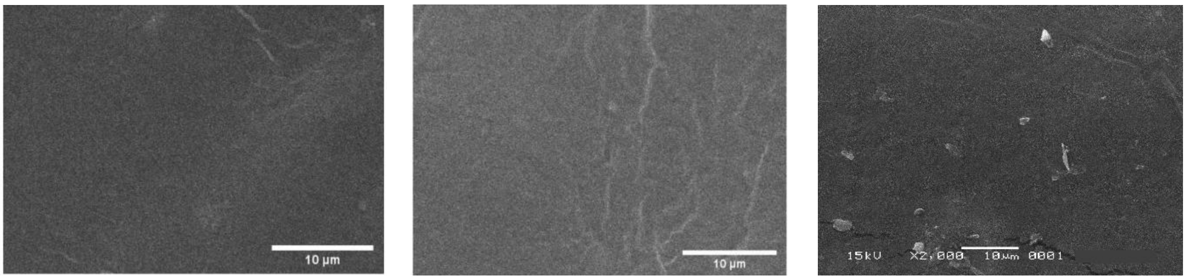

(*a*) (*b*) (*c*)

Figure 7. SEM image of (*a*) pectin, (*b*) pectin/PVP, (*c*) pectin/PVP/CNC films

In contrast, the pectin/PVP (7:1) polyblend film exhibits a smoother and more homogeneous surface morphology with no visible phase separation. The absence of distinct domains or cracks indicates good miscibility between pectin and PVP, which can be attributed to strong intermolecular hydrogen bonding between the hydroxyl groups of pectin and the carbonyl groups of PVP. This homogeneous morphology corroborates the FTIR evidence of polymer–polymer interactions and explains the improved mechanical balance of strength and flexibility in the polyblend film.

Upon incorporation of CNC into the pectin/PVP matrix, the surface morphology shows noticeable changes. The pectin/PVP/CNC nanocomposite films display a slightly roughened surface compared to the polyblend, with fine granular features uniformly distributed across the surface. No large CNC agglomerates or phase-separated regions are observed, indicating a reasonably good dispersion of CNC within the polymer matrix. The increased surface roughness is attributed to the presence of CNC and polymer–CNC interfacial regions, which disrupt the smooth polymer surface while maintaining overall film integrity.

The evolution of surface morphology with CNC incorporation is consistent with the observed mechanical and thermal behavior. The introduction of CNC-induced interfacial heterogeneity contributes to enhanced ductility at lower CNC loadings and partial recovery of stiffness at higher CNC content, as well as to the modulation of segmental mobility evidenced by DSC analysis. From the perspective of solid polymer electrolyte matrices, the absence of macroscopic defects and the presence of a continuous polymer phase are essential for maintaining electrode–electrolyte contact and mechanical stability during operation.

The combined FTIR, DSC, SEM, and mechanical analyses reveal a coherent structure–property mechanism governing the behavior of the pectin/PVP/CNC nanocomposites. FTIR results demonstrate that the system is dominated by hydrogen-bond-mediated interactions, where blending pectin with PVP reorganizes the original polysaccharide network into a more homogeneous matrix, while CNC incorporation introduces additional hydroxyl-rich interfacial domains without forming new covalent bonds. These molecular interactions directly influence chain dynamics, as evidenced by DSC, where the T_g-related enthalpy relaxation and its evolution with CNC content reflect a tunable balance between segmental mobility and structural constraint. SEM observations further confirm that this balance is achieved through good matrix continuity and uniform CNC dispersion, with no macroscopic phase separation or agglomeration that could compromise mechanical integrity. Consequently, the mechanical response of the films transitions from a rigid and brittle behavior (neat pectin) to an optimized combination of strength and ductility (pectin/PVP), followed by a CNC-modulated response in which low filler loading enhances compliance while higher loading restores stiffness.

The confirmed formation of cellulose nanocrystals with well-defined morphology and nanoscale dimensions provides a robust nanofiller platform for tailoring the structure and properties of pectin/PVP matrices. The combined results from FTIR, DSC, SEM, and mechanical analysis consistently demonstrate that CNC incorporation modulates hydrogen-bond interactions, segmental mobility, and microstructural homogeneity in a composition-dependent manner. At intermediate CNC loadings, enhanced chain mobility contributes to improved ductility, while higher CNC contents partially restore stiffness and mechanical integrity without inducing crystallinity. This tunable balance between flexibility and structural stability highlights the ability of CNC to regulate the intermolecular network of the polymer matrix. These findings establish a clear structure–property relationship and indicate that the pectin/PVP/CNC system represents a promising platform for further development of functional biopolymer-based materials, including future exploration in solid polymer electrolyte systems.

Conclusions

This study demonstrates that pectin/PVP/CNC nanocomposites constitute a tunable biopolymer platform whose structural interactions and thermal–mechanical responses can be systematically tailored through controlled CNC incorporation. The results show that hydrogen-bond-mediated interactions govern the organization of the polymer network, enabling modulation of segmental mobility, relaxation behavior, and mechanical integrity without inducing crystallinity or phase separation. The optimized balance between compliance and stiffness, together with preserved amorphous character and thermal stability, highlights the suitability of the pectin/PVP/CNC system as a sustainable matrix for solid polymer electrolytes. These findings provide a mechanistic basis for the rational design of bio-based electrolyte matrices and open pathways for further optimization through salt incorporation and electrochemical performance evaluation. Future work will focus on lithium salt incorporation to evaluate the electrochemical window, ionic conductivity, and cycling stability of the pectin/PVP/CNC-based solid polymer electrolytes.

Funding

This work was supported by the Directorate of Research and Community Service Universitas Pendidikan Indonesia through the Strengthening Research Groups Scheme 2025 (Contract Number: 443/UN40/PT.01.02/2025). The authors have no competing interests to declare that are relevant to the content of this article.

Data Availability

The data that support the findings of this study are available from the corresponding authors upon reasonable request.

*Author Information**

**The authors' names are presented in the following order: First Name, Middle Name and Last Name*

Budiman Anwar (*corresponding author*) — Doctor of Material Chemistry, Head of ChemTransform for Sustainability Research Group, Associate Professor at Chemistry Programs, Universitas Pendidikan Indonesia, Jl. Dr. Setiabudhi No. 229, Bandung, Indonesia; e-mail: budimananwar@upi.edu; https://orcid.org/0000-0001-8085-9568

Lidya Intan Febriani — Bachelor of Chemistry, Junior Researcher, Chemistry Programs, Universitas Pendidikan Indonesia, Jl. Dr. Setiabudhi No. 229, Bandung, Indonesia; e-mail: lidiainfeb@gmail.com

Fitri Dara — Doctor of Chemistry, Senior Researcher, National Research and Innovation Agency (BRIN), Prof. Dr. Samaun Samadikun Science and Technology Area (KST), Jl. Sangkuriang, Bandung, Indonesia; e-mail: fitr002@brin.go.id; https://orcid.org/0000-0003-2678-4248

Galuh Yuliani — Doctor of Chemistry, Senior Lecturer, Chemistry Programs Universitas Pendidikan Indonesia, Jl. Dr. Setiabudhi No. 229, Bandung, Indonesia; e-mail: galuh@upi.edu; https://orcid.org/0000-0003-4291-6618

Author Contributions

The manuscript was written through contributions of all authors. All authors have given approval to the final version of the manuscript. CRediT: **Budiman Anwar** conceptualization, data curation, funding acquisition, resources, supervision, validation, writing-original draft, writing-review & editing; **Lidya Intan Febriani** investigation, formal analysis, visualization; **Fitri Dara** data curation, formal analysis, resources; **Galuh Yuliani** data curation, formal analysis, funding acquisition, writing-review & editing.

Acknowledgments

The authors would like to express their sincere appreciation to the Directorate of Research and Community Service Universitas Pendidikan Indonesia for the financial support.

Conflicts of Interest

The authors declare no conflict of interest.

References

1 Ma, C., Cui, W., Liu, X., Ding, Y., & Wang, Y. (2022). In situ preparation of gel polymer electrolyte for lithium batteries: Progress and perspectives. *InfoMat, 4*(2), e12232. https://doi.org/10.1002/inf2.12232

2 Song, Y., Su, M., Xiang, H., Kang, J., Yu, W., Peng, Z., Wang H., Cheng B., Deng, N., & Kang, W. (2025). PEO-based solid-state polymer electrolytes for wide-temperature solid-state lithium metal batteries. *Nano-Micro Small, 21*(3), 2408045. https://doi.org/10.1002/smll.202408045

3 Khan, K.H., Haleem, A., Arwish, S., Shah, A., & Hussain, H. (2025) PVDF-based solid polymer electrolytes for lithium-ion batteries: strategies in composites, blends, dielectric engineering, and machine learning approaches. *RSC Advanced, 15,* 20629-20656. https://doi.org/10.1039/d5ra02951a

4 Chen, T., Zhao, F., Wang, L., Ma, S., Shi, G., Liu, Q., Liu, Y., & Han, G. (2025). High-performance PMMA based solvent-free solid transparent polymer electrolyte modified by succinonitrile for electrochromic devices. *Solar Energy Materials and Solar Cells, 285,* 113538. https://doi.org/10.1016/j.solmat.2025.113538

5 Dennis, J.O., Shukur, M.F., Aldaghri, O.A., Ibnaouf, K.H., Adam, A.A., Usman, F., Hassan, Y.M., Alsadig, A., Danbature, W.L., & Abdulkadir, B.A. (2023). A Review of current trends on poly(vinyl alcohol) (PVA)-based solid polymer electrolytes. *Molecules, 28*(4), 1781. https://doi.org/10.3390/molecules28041781

6 Kumar, L.S., Selvin, P.C., & Selvasekarapandian, S. (2021). Impact of lithium triflate ($LiCF_3SO_3$) salt on tamarind seed polysaccharide-based natural solid polymer electrolyte for application in electrochemical device. *Polymer Bulletin, 78,* 1797–1819. https://doi.org/10.1007/s00289-020-03185-5

7 Rani, M.S., Rudhziah, S., Ahmad, A., & Mohamed, N.S. (2014). Biopolymer electrolyte based on derivatives of cellulose from kenaf bast fiber. *Polymers 6*(9), 23712385. https://doi.org/10.3390/polym6092371

8 Adlin, H.P., Ajith, K., Infanta, D.M., Lakshmi, D., & Christopher, S.P. (2022). Chitosan-based biopolymer electrolyte reinforced with V_2O_5 filler for magnesium batteries: an inclusive investigation. *Journal of Materials Science: Materials in Electronics 33*(7), 3925–3937. https://doi.org/10.1007/s10854-021-07587-7

9 Nešić, A., Ružić, J., Gordić, M., Ostojić, S., Micić, D., & Onjia, A. (2017). Pectin-polyvinylpyrrolidone films: A sustainable approach to the development of biobased packaging materials. *Composites Part B: Engineering 110,* 56-61. https://doi.org/10.1016/j.compositesb.2016.11.016

10 Ilyas, R.A., Sapuan, S.M., Sanyang, M.L., Ishak, M.R., & Zainudin, E.S. (2018). Nanocrystalline cellulose as reinforcement for polymeric matrix nanocomposites and its potential applications: A review. *Current Analytical Chemistry, 14*(3), 203–225. https://doi.org/10.2174/1573411013666171003155624

11 Xu, X., Liu, F., Jiang, L., Zhu, J.Y., Haagenson, D., & Wiesenborn, D.P. (2013). Cellulose nanocrystals vs. cellulose nanofibrils: A comparative study on their microstructures and effects as polymer reinforcing agents. *ACS Applied Materials & Interfaces, 5*(8), 2999–3009. https://doi.org/10.1021/am302624t

12 Anwar, B., Bundjali, B., & Arcana, I.M. (2015). Isolation of cellulose nanocrystals from bacterial cellulose produced from pineapple peel waste juice as culture medium. *Procedia Chemistry*, *16*, 279–284. https://doi.org/10.1016/j.proche.2015.12.051

13 Anwar, B., Bundjali, B., Sunarya, Y., & Arcana, I.M. (2021). Properties of bacterial cellulose and its nanocrystalline obtained from pineapple peel waste juice. *Fibers and Polymers*, *22*, 1228–1236. https://doi.org/10.1007/s12221-021-0765-8

14 Segal, L., Creely, J.J., Martin, Jr. A.E., & Conrad, C.M. (1959). An empirical method for estimating the degree of crystallinity of native cellulose using the X-ray diffractometer. *Textile Research Journal, 29,* 786–794. https://doi.org/10.1177/004051755902901003

15 Nelson, M.L. & O'Connor, R.T. (1964). Relation of certain infrared bands to cellulose crystallinity and crystal lattice type. Part II. A new infrared ratio for estimation of crystallinity in celluloses I and II. *Journal of Applied Polymer Science*, *8*(3), 1325–1341. https://doi.org/10.1002/app.1964.070080323

16 Thakur, M., Sharma, A., Ahlawat, V., Bhattacharya, M., & Goswami, S. (2020). Process optimization for the production of cellulose nanocrystals from rice straw derived α-cellulose. *Materials Science for Energy Technologies, 3,* 328–34. https://doi.org/10.1016/j.mset.2019.12.005

17 Newman, R.H. (1999). Estimation of the lateral dimensions of cellulose crystallites using ^{13}C NMR signal strengths. *Solid State Nuclear Magnetic Resonance, 15*(1), 21–29. https://doi.org/10.1016/S0926-2040(99)00043-0

18 French, A.D. & Cintron, M.S. (2013). Cellulose polymorphy, crystallite size, and the Segal Crystallinity Index. *Cellulose, 20,* 583–588. https://doi.org/10.1007/s10570-012-9833-y

19 Lewandowska, K. & Szulc, M. (2021). Characterisation of hyaluronic acid blends modified by poly(*N*-vinylpyrrolidone). *Molecules*, *26*(17), 5233 https://doi.org/10.3390/molecules26175233

20 Hazrati, K.Z., Sapuan, S.M., Zuhri, M.Y.M., & Jumaidin, R. (2021). Effect of plasticizers on physical, thermal, and tensile properties of thermoplastic films based on *Dioscorea hispida* starch. *International Journal of Biological Macromolecules*, *185*, 219–228. https://doi.org/10.1016/j.ijbiomac.2021.06.099

21 Sanyang, M.L., Sapuan, S.M., Jawaid, M., Ishak, M.R., & Sahari, J. (2015). Effect of plasticizer type and concentration on tensile, thermal and barrier properties of biodegradable films based on sugar palm (*Arenga pinnata*) starch. *Polymers*, *7*(6), 1106–1124; https://doi.org/10.3390/polym7061106

22 Garavito, J., Castellanos-González, S., Peña-Venegas, C.P., & Castellanos, D.A. (2026). Development and characterization of reinforced flexible packaging based on amazonian cassava starch through flat sheet extrusion. *Polymer*, *18*(6), 675, 1–24. https://doi.org/10.3390/polym18060675

23 Shi, S., Wang, Y., Zhang, Y. et al. (2023). Plasticizer role of cellulose nanocrystals in the biodegradable polymer blend with ductile polymer as continuous phase. *Cellulose*, *30*, 10139–10156. https://doi.org/10.1007/s10570-023-05501-4

24 Ding, C., Zhang, M., & Li, G. (2015). Preparation and characterization of collagen/hydroxypropyl methylcellulose (HPMC) blend film. *Carbohydrate Polymers*, *119*, 194. http://dx.doi.org/10.1016/j.carbpol.2014.11.057

25 Voronova, M., Rubleva, N., Kochkina, N., Afineevskii, A., Zakharov, A., & Surov, O. (2018). Preparation and characterization of polyvinylpyrrolidone/cellulose nanocrystals composites. *Nanomaterials*, *8*(12), 1011. https://doi.org/10.3390/nano8121011

26 Yu, Y., Tyrikos-Ergas, T., Zhu, Y., et al. (2019). Systematic hydrogen-bond manipulations to establish polysaccharide structure–property correlations. *Angewandte Chemie, 58*(37), 13127–13132. https://doi.org/10.1002/anie.201906577

27 Kawai, K., Sogabe, T., Nakagawa, H., Yamada, T., & Koseki, S. (2024). Effect of water activity on the mechanical glass transition and dynamical transition of bacteria-solute systems. *Journal of Food Engineering 375,* 112066. https://doi.org/10.1016/j.jfoodeng.2024.112066

28 Anwar, B., Nurhashiva, C., Arwa, R., & Yuliani, G. (2023). Physicochemical properties of bioplastic based on hydroxyethylcellulose and polyvinylpyrrolidone blend. *Journal of the Serbian Chemical Society*, *89*, 215–30. https://doi.org/10.2298/jsc231023103a

29 Sydykov, B., Oldenhof, H., Sieme, H., & Wolkers, W.F. (2017). Hydrogen bonding interactions and enthalpy relaxation in sugar/protein glasses. *Journal of Pharmaceutical Sciences*, *106*(3), 761–769. https://doi.org/10.1016/j.xphs.2016.11.003